

In-situ X-ray observations and microstructural characterizations for understanding combustion foaming and reaction processes to synthesize porous Al₃Ti composites from Al-Ti-B₄C powders.

Takamasa Inukai, Asuka Suzuki, Naoki Takata, Makoto Kobashi, Yuji Okada, and Yuichi Furukawa*

Takamasa Inukai, Dr. Asuka Suzuki, Prof. Naoki Takata, Prof. Makoto Kobashi
Department of Materials Process Engineering, Graduate School of Engineering, Nagoya
University, Furo-cho, Chikusa-ku, Nagoya, 464-8603 Japan.
E-mail: suzuki.asuka@material.nagoya-u.ac.jp

Yuji Okada, Yuichi Furukawa
TOYOTA MOTOR CORPORATION, 1 Toyota-cho, Toyota, 471-8571 Japan.

Declarations of interest: None

Keywords: Porous metal; Intermetallic; Aluminide; Combustion reaction; X-ray radiography

Abstract

The combustion foaming behaviors to synthesize closed-cellular porous Al_3Ti composites are observed in situ using X-ray radiography. The in-situ observation of the thermal explosion (TE) mode foaming reveals that the combustion foaming process consists of six steps. The shape of the sample changes uniformly in the first three steps before the sample foams. First, the sample expands uniformly ((1) gradual expansion) and maintain an almost constant volume for a fixed period ((2) temporary steady state at a constant volume). During these stages, bubbles are not generated inside the sample. Subsequently, the sample shrinks uniformly ((3) slight shrinkage). After these three steps, the bubbles are rapidly generated inside the sample ((4) rapid foaming). Immediately after foaming, the sample shrinks drastically while bubbles are ruptured and combined ((5) severe shrinkage and bubble coarsening). Finally, the sample solidifies as a porous metal ((6) solidification). The sample fabricated under the self-propagating high-temperature synthesis (SHS) mode includes graded microstructures corresponding to steps (1)–(4). The microstructures of the samples foamed under the TE and SHS modes are characterized. These results are used for discussing the elementary reaction steps arising at steps (1)–(4).

1. Introduction

Porous metals include a lot of pores inside the materials. Due to the pores, they exhibit unique properties such as ultra-light weight, low thermal conductivity, high specific stiffness, and high impact energy absorption capacity [1–4]. Transition metal aluminides (Al_mX_n ($X=Ti, Ni, Fe,$ etc.)) have many attractive characteristics and are used for structural applications under severe environments [5–7]. For example, titanium trialuminide (Al_3Ti) has low density ($3.4\text{ g}\cdot\text{cm}^{-3}$), high Vickers microhardness (465–670 HV), high Young's modulus (215.7 GPa), strong oxidation resistance even at $1000\text{ }^\circ\text{C}$, and high melting temperature (approximately $1340\text{ }^\circ\text{C}$) [8, 9]. Therefore, porous Al_3Ti , possesses both the unique properties of porous metals and attractive material characteristics, can be used for members for reinforcing stiffness and thermal barrier coatings at high temperatures [10].

One of the promising routes to synthesize the transition metal aluminides is the combustion reaction [11]. In the combustion reaction, ceramics and intermetallics with high melting temperatures can be synthesized effectively by chemical reactions generating a large amount of heat. Open-cellular porous aluminides can be fabricated by a combined process of the combustion reactions and space holder method [12–14]. In this method, raw powders are mixed with space holder particles and are reacted, followed by the removal of the space holder particles. The porosity and pore morphology can be controlled by the amount and shape of the space holder particles. On the other hand, Inoguchi et al. [10] and Kobashi et al. [15] developed a combustion foaming process that enables the fabrication of closed-cellular porous intermetallic composites by controlling the combustion reactions. In the combustion foaming process, exothermic agents are added to control the total reaction heat and assist the reaction progress. For example, the combustion reactions to synthesize porous Al_3Ti composites from a mixture of B_4C powder and elemental powders of Al and Ti (hereafter denoted as Al–Ti– B_4C powders) are described in the following Eqs. (1) and (2).



Al and Ti react to form Al_3Ti , as shown in Equation (1). The exothermic agent B_4C also reacts with Ti to form TiB_2 and TiC and generates a large amount of reaction heat. When a precursor composed of Al–Ti– B_4C powders is heated, two combustion reactions are triggered at the melting temperature of Al (approximately 660 °C) [10]. **Figure 1 (a)** shows the change in the total reaction heat as a function of the total volume fraction of $\text{TiB}_2 + \text{TiC}$ after the reactions, which corresponds to the additive amount of the exothermic agent [16]. The reaction heat was calculated assuming that the reaction starts at the melting temperature of Al. The total reaction heat increases with an increase in the additive amount of the exothermic agent, indicating that the reaction heat can be controlled by the additive amount of the exothermic agent. It is suggested that the closed-pores are formed during the reactions by the gas released from the hydrous oxide ($\text{Al}_2\text{O}_3 \cdot 3\text{H}_2\text{O}$) on the surface of Al powder and/or hydrogen dissolved in Al powder [17, 18].

The combustion reaction is categorized in two different modes: (1) thermal explosion (TE) mode and (2) self-propagating high-temperature synthesis (SHS) mode [19–22]. In the TE mode, the entire sample is heated uniformly so that the reaction occurs simultaneously throughout the sample. In the SHS mode, one end of a long-scale precursor is heated locally to induce the combustion reaction. Then, the heat of the reaction transfers to the neighboring zone and triggers the combustion reaction again. The reaction propagates spontaneously throughout the precursor, from the heated end to the non-heated end.

Porosity and pore morphology are important factors to control the properties of porous metals such as thermal conductivity, strength, modulus, and impact energy absorption capacity [1]. However, the combustion foaming process is not sufficiently understood because the combustion reaction proceeds rapidly and irreversibly. To control the porosity and pore

morphology, the foaming process needs to be clarified. The foaming process of porous Al and Al alloys using a TiH_2 blowing agent has been investigated using in-situ X-ray radioscopy [23, 24]. Furthermore, three-dimensional images of porous Al during the foaming process have been recently obtained by performing in-situ synchrotron X-ray tomography [25, 26]. Thus, the in-situ observations using X-rays are an effective method for understanding the foaming behavior. Furthermore, Arakawa et al. reported the combustion foaming behavior in the Al-Ti- B_4C system using the synchrotron X-ray radioscopy [27], providing insight into an immediate pore coarsening process after foaming. However, the relationship between the foaming behavior and the elementary steps of the combustion reaction has not been understood using only in-situ X-ray observations.

In the present study, the combustion foaming behaviors under the TE and SHS modes were observed in situ using X-ray radioscopy. The microstructures in the samples foamed under these modes were characterized in detail. By combining the in-situ observations and microstructural characterizations, the dominant steps of the elementary reactions in the combustion foaming behaviors are discussed.

2. Experimental procedure

2.1 Materials

Al (purity > 99.99%, particle size < 45 μm), Ti (purity: 99.9%, particle size < 45 μm), and B_4C (purity > 99%, average particle size: 0.5 μm) powders were used as initial materials. **Figure 2** shows the secondary electron images (SEIs) of the initial powders used in this study. In the present study, the molar ratio of Al: Ti: B_4C was fixed at 2.32: 1.00: 0.07, where Al_3Ti , TiB_2 , and TiC phases were expected to be formed in the equilibrium condition. The total volume fraction of TiB_2 and TiC is expected to be 10 vol.% after the reactions. Figure 1 (b, c) presents the changes in (b) the adiabatic combustion temperature and (c) melting fraction of the Al_3Ti phase as a function of the volume fraction of TiB_2+TiC . The adiabatic combustion temperature

and melt fraction of Al_3Ti were calculated using Equation (3) based on previously reported thermodynamic databases [16, 28, 29]. It is assumed here that the reactions proceed under an adiabatic condition, and that the reaction heat is consumed only to raise the sample temperature.

$$\Delta H_r(T_{\text{ig}}) = \begin{cases} \int_{T_{\text{ig}}}^{T_{\text{ad}}} C_p^S dT & (T_{\text{ad}} < T_m) \\ \int_{T_{\text{ig}}}^{T_{\text{ad}}} C_p^S dT + \nu \Delta H_m & (T_{\text{ad}} = T_m) \\ \int_{T_{\text{ig}}}^{T_m} C_p^S dT + \Delta H_m + \int_{T_m}^{T_{\text{ad}}} C_p^L dT & (T_{\text{ad}} > T_m) \end{cases} \quad (3)$$

where T_{ig} and T_{ad} are the ignition temperature and adiabatic combustion temperature, respectively. $\Delta H_r(T_{\text{ig}})$ is the enthalpy of the reaction induced at T_{ig} . C_p^S and C_p^L are the heat capacities of the reaction product in the solid and liquid states, respectively. ΔH_m is the enthalpy of fusion of the product. ν is the melt fraction of the product ($0 \leq \nu \leq 1$). The broken line in Figure 1 indicates the composition in this study. It is expected that the adiabatic combustion temperature reaches the melting temperature of the Al_3Ti phase, and that approximately 87% of Al_3Ti phase melts. After dry-mixing the raw powders for 1800 s, Al–Ti– B_4C powders were compacted using uniaxial cold pressing (200 MPa) to fabricate cylindrical precursors having two different shapes of cylindrical precursors: (1) 20 mm in diameter and 8 mm in height, and (2) 15 mm in diameter and 15 mm in height. The precursors of (1) and (2) were foamed under the TE and SHS modes, respectively.

2.2 In-situ observations of foaming behaviors

To observe the foaming behavior in situ, the samples were irradiated with X-rays while being inductively heated. **Figure 3 (a)** shows the schematic illustration of the set-up used to observe the foaming behavior in situ by X-ray radioscopy. The sample was irradiated with X-rays operated at 49 kV and 13 mA through the quartz glass window and the gap between the adjacent induction coils (2 mm). The X-ray transmitting the sample passed through the gap and glass at the opposite side of the X-ray source and was applied to an image intensifier. The intensified

images were recorded using a charge-coupled device (CCD) camera. Most of the detected X-ray were X-ray transmitting through the sample, and scattered and reflected X-rays were negligible.

The samples were heated under an Ar gas atmosphere (5.0×10^4 Pa) in different two different ways: the TE and SHS modes. When the sample with 20 mm in diameter and 8 mm in height was heated in the TE mode, the sample was set in a graphite mold (Figure 3 (b)). The thermal insulator was set under the sample. The thermal insulator permits preventing heat transfer from the bottom surface of the graphite mold, which is preferentially inductively heated, and heating the sample uniformly. Ar gas was introduced because Ar gas atmosphere is preferable to vacuum to obtain high porosity products [30]. The apparatus used in the present study was designed to be used only under negative pressures. Considering the increase in the internal pressure at elevated temperature, 5.0×10^4 Pa was selected. The heating rate was controlled at $1.0 \text{ }^\circ\text{C} / \text{s}$, while the temperature in the furnace was monitored with a thermocouple, as shown in Figure 3 (b). Higher heating rate causes the non-uniform temperature distribution inside the sample, while lower heating rate causes the solid-solid reaction before foaming and prevents rapid foaming. Based on these balances, the heating rate of $1.0 \text{ }^\circ\text{C} / \text{s}$ was selected. After the precursor was foamed, heating was stopped, followed by furnace cooling to ambient temperature.

To evaluate the foaming behavior quantitatively, the images observed in situ under the TE mode were analyzed using a software (ImageJ, National Institutes of Health, NIH). The outline of the sample was quantified as the projected area.

To measure the sample temperature during the foaming process, a thermocouple was inserted into another precursor with 20 mm in diameter and 8 mm in height (Figure 3 (c)). The precursor was foamed under the same conditions as above. The insertion of the thermocouple can affect

the foaming behavior. Therefore, when the sample temperature was measured, only the projected area was evaluated although the foaming behavior was observed in situ.

When the sample with 15 mm in diameter and 15 mm in height was heated in the SHS mode, the sample was placed on a graphite plate (Figure 3 (d)). The same atmosphere and heating rate as TE mode foaming were applied. The bottom surface of the sample was preferentially heated by heat transfer from the graphite plate, which was heated rapidly. Heating was stopped when the combustion foaming behavior started, followed by furnace cooling to ambient temperature.

2.3 Microstructural characterizations

After the samples were cut, they were soaked in an epoxy resin, after which the resins were cured. The cross-sections were mechanically polished and buffed with diamond slurries (3 μm), followed by final polishing with colloidal silica (0.25 μm). Os was deposited on the polished surface to prevent charge-up on the epoxy resins. The microstructures of the samples were observed using scanning electron microscopy (SEM). The chemical compositions were analyzed with energy dispersive X-ray spectroscopy (EDS). The element maps were obtained under 20 kV, and line analysis was performed under 10 kV.

X-ray diffraction (XRD) measurements were conducted using a Cu-K α radiation source (wavelength: $\lambda = 0.15405$ nm) operated at 40 kV and 40 mA to identify constituent phases. To obtain clear diffraction peaks, the sample foamed under the TE mode was crushed to powder and compacted to a bulk. The bulk was embedded into the epoxy resin and polished to expose all the constituent phases to the surface.

The sample fabricated under the TE mode was cut into a small piece and ion-polished using a cross-section polisher at 5 V. The microstructure was observed using field emission SEM (FE-SEM) operated at 20 kV. The constituent phases were identified by performing electron back-scatter diffraction (EBSD) analyses.

3. Results

3.1 TE-mode foaming behavior

Figure 4 shows (a – l) X-ray radiography images showing the foaming process of the TE mode sample at (a) 0.0 s, (b) 5.4 s, (c) 10.0 s, (d) 15.0 s, (e) 17.4 s, (f) 18.1 s, (g) 18.6 s, (h) 19.1 s, (i) 19.9 s, (j) 20.9 s, (k) 23.5 s, and (l) 59.7 s and (m) projected area normalized by the projected area of the precursor in (a) as a function of time. The time was defined as 0 s when the volume change of the precursor was observed. When a foam is liquid, a pore is denoted as a bubble and a cell wall is described as a film in the explanations below. First, the precursor was expanded to be approximately 1.3 times as large without any significant change in the shape (Figure 4 (a–c, m)). Subsequently, the sample's shape remained constant for approximately 10 s (Figure 4 (c, d, m)). The sample shrank to almost the original size at 17.4 s (Figure 4 (e, m)) and was then suddenly foamed (Figure 4 (f–h, m)). During the foaming, bubbles were generated and grew rapidly (Figure 4 (f–h)). The normalized projected area became approximately three times larger than that of the precursor in Figure 4 (a) (Figure 4 (m)). After the maximum foaming, the sample shrank to a normalized projected area of approximately 2.5 (Figure 4 (h–k)). The liquid films were ruptured (broken circles in (h, i)) and coarsened during the shrinkage. Even when the shrinkage was almost converged, the coarsening behavior continued (broken circles in (k, l)). After 60 s, bubbles remained as pores inside the solidified sample. Thus, the combustion foaming process consisted of six steps: (1) gradual expansion, (2) temporary steady state at a constant volume, (3) slight shrinkage, (4) rapid foaming, (5) severe shrinkage and bubble coarsening, and (6) solidification.

Figure 5 shows (a) a photograph of the cross-section and (b) the XRD profile of the sample foamed under the TE mode. As observed in Figure 5 (a), the foamed sample had coarsened pores, which corresponds to the porous structure observed in Figure 4 (l). The porosity of this sample measured using the Archimedes' method was 79.6%. Only the peaks of the Al_3Ti (D0₂₂

structure)[31] and TiB_2 (C32 structure) [32] phases were detected (Figure 5 (b)). The peaks of TiC (B1 structure) [33] phase were not detected owing to the small volume fraction of TiC (the theoretical volume fraction of TiC is 2.8vol.%). Peaks for unreacted phases such as $\alpha\text{-Al}$, $\alpha\text{-Ti}$, B_4C , and intermediate products such as TiAl , Ti_3Al , and TiB were not detected, indicating that the reactions were almost completed.

Figure 6 shows (a) low- and (b) high-magnification backscattered electron images (BEIs) showing the microstructure and (c-f) EDS element maps of (c)Al, (d)Ti, (e) B, and (f) C in the cell wall of the sample foamed under the TE mode. In Figure 6 (a), the darkest contrast corresponds to the pores. In the magnified microstructure (Figure 6 (b)), it was observed that the needle-shaped particles with bright contrast were aggregated in the matrix with dark contrast. In the matrix, Al and Ti were detected, suggesting that the matrix was Al_3Ti phase. Ti, B, and C were preferentially detected in the needle-shaped particles. It is considered that the particles were TiB_2 or TiC phases.

Figure 7 presents (a) the FE-SEM image of porous Al_3Ti composite fabricated under the TE-mode foaming showing EBSD analysis points, (b, d) EBSD patterns from the points shown in (a), and (c, e) their fitted images. The EBSD patterns in (b, d) were fitted by crystalline structures of Al_3Ti and TiB_2 phases, respectively [31, 32]. The confidence index (CI) values [34], which indicate the accuracy of indexing EBSD patterns, are 0.42 and 0.11 for Al_3Ti and TiB_2 phases, respectively. This result indicates the high reliability of the analyzed results. Thus, it is confirmed that the matrix was the Al_3Ti phase, and needle-shaped particles were the TiB_2 phase. The presence of the TiC phase was not confirmed in the present study, and further investigations are needed.

Figure 8 shows the change in the normalized projected area and the temperature measured with the thermocouple inserted into the sample. The broken line indicates the change in the temperature before the combustion foaming behavior (gradual expansion) started, that is, temperature change controlled by induction heating. The foaming behavior started at

approximately 660 °C, that is, the melting temperature of Al, which was in good agreement with previous studies [[10]]. Even after the expansion started, the temperature increased almost linearly with the same slope as before the expansion. The temperature rise deviated largely from the broken line around the end of the temporary steady state (around 25 s in Figure 8). The temperature started to increase drastically at the slight shrink stage (around 30 s in Figure 8). The sample temperature reached the melting temperature of Al₃Ti (1340°C) during foaming and stayed at approximately 1340°C when the sample shrank severely, followed by gradual cooling. The maximum temperature was in good agreement with the calculated adiabatic combustion temperature in Figure 2 (b).

3.2. SHS-mode foaming behavior

Figure 9 shows X-ray radiography images showing foaming process of the SHS mode sample (a) 0.0 s, (b) 50.0 s, (c) 60.0 s, (d)70.0 s, (e)86.0 s (f) 87.0 s, (g) 88.0 s, (h) 90.0 s, (i) 93.0 s, (j)100 s, (k)120.0 s, and (l)180.0 s. The broken line indicates that outline of the precursor shown in Figure 9 (a). First, the sample was expanded from the lower part (Figure 9 (b)). The expansion was propagated to the upper part (Figure 9 (c–e)), followed by the foaming of the upper part ((Figure 9 (f)). Just below the foamed part, the sample slightly shrank (Figure 9 (f)). The sample did not foam entirely, and the combustion reaction quenched. It should be noted that the sample was foamed from the top, although the expansion started from the bottom.

Figure 10 shows (a) a photograph of the sample foamed under the SHS mode and (b–f) BEIs showing the microstructures in (b) precursor and (c–f) regions (i)–(iv) shown in (a). As shown in Figure 10 (b), Ti particles were surrounded by the Al matrix in the precursor. The relative density of the precursor was approximately 85%, and the precursor did not have large voids. In the upper part of the sample foamed under the SHS mode, large pores were observed (Figure 10 (a)). The pores were generated by the foaming at the upper part observed in Figure 9. In the sample, roughly four types of microstructures were observed. In region (i) (the bottom part),

voids were observed, which were absent from the precursor shown in Figure 10 (b). The bright phases were surrounded by the darker phase. In the darker phase, the aggregated particles were observed. In these images, the bright, intermediate, and dark-contrast areas as well as the dark-contrast particles correspond to α -Ti, Ti_3Al , Al_3Ti and B_4C phases, respectively. In region (ii), a microstructure similar to that in region (i) was observed, but needle-shaped particles (TiB_2) were formed. In region (iii), almost all the voids disappeared. The amount of the TiB_2 phase increased significantly compared with region (ii). The interface between the bright particles and the matrix was blurred, which is an indicator of melting of the matrix and dissolution of elements from the bright particles into the liquid phase. In region (iv), the Al_3Ti matrix and TiB_2 particles were observed, which was a microstructure similar to the sample foamed under the TE mode.

Figure 11 presents the XRD profile measured in region (i). This profile was measured by masking other regions with a non-crystalline tape. The peaks of α -Ti (hcp, (A3 structure)) [35], B_4C (D1_g structure) [36], Al_3Ti (D0_{22} structure) [31], Ti_3Al (D0_{19} structure)[37], and TiB_2 (C32 structure) [32] were detected. **Figure 12** shows (a) BEI, (b–e) EDS element maps of (b) Al, (c) Ti, (d) B, and (e) C, and (f) concentration profiles of Al and Ti measured along the white arrow in (a) in region (i). In the bright particle, Ti was strongly detected while Al was preferentially detected in the darker matrix phase. As shown in Figure 12 (f), the brightest core consisted of approximately 100 mol% Ti, indicating that the core was the α -Ti phase. A slightly darker phase around the α -Ti phase consisted of approximately 63 mol% Ti and 37 mol% Al. Considering the XRD profile shown in Figure 11 and the equilibrium phase diagram for the Al–Ti binary system [38], the phase was Ti_3Al . The formation of Ti_3Al during the combustion reactions in the Al–Ti– B_4C system was reported in the literature [39]. The matrix consisted of approximately 75 mol% Al and 25 mol% Ti, indicating that the phase was Al_3Ti [38]. It should be noted that the change in the concentration at the interface between the Ti_3Al and Al_3Ti phases

was discontinuous (sharp interface). In addition, in the aggregated darker particles, B and C were detected while Ti and Al were hardly detected, indicating the particles of the B_4C phase.

Figure 13 shows the high-magnification BEI showing the microstructure in the region (ii) shown in Figure 10 (d). Needle-shaped TiB_2 was formed on the B_4C and Al_3Ti phases, indicating that TiB_2 was not formed via the reaction between Ti and B_4C , as described in Equation (2). **Figure 14** shows (a) high-magnification BEI showing the microstructure in the region (iii) shown in Figure 10 (e) and (b) concentration profiles of Al and Ti along the white arrow shown in (a). The change in the chemical composition at the interface between the Al_3Ti matrix and Ti_3Al appeared continuous (blurred interface). In addition, the concentration changed gradually depending on the position in the Ti_3Al phase, indicating that the sample solidified while the elements were dissolved into molten Al-Ti. The sample was partially molten in region (iii).

4. Discussion

First, when the sample was foamed under the SHS mode, the expansion started from the bottom of the sample (heated end) (Figure 9 (b)), whereas foaming occurred from the top (Figure 9 (f)). The SHS-mode foaming process will be discussed based on microstructural observations. **Figure 15** presents a schematic illustration showing heat flow during the SHS foaming process observed in situ by X-ray radioscopy. The expansion started from the melting temperature of Al (660 °C) (Figure 8). In the bottom part which experienced only the expansion (Figure 9), Al_3Ti and Ti_3Al phases were formed while TiB_2 was hardly formed (Figs. 10 (c), 11, and 12). These results indicate that the sample expanded by the reaction between liquid Al and Ti (the reaction described by Equation (1)). Hibino et al. reported that the combustion reaction of Al-Ti system proceeded at the interface between the Ti powder and molten Al, which generated numerous voids resulting in an expansion of the sample [40]. The bottom of the SHS mode sample was heated preferentially via heat transfer from the carbon plate (Figure

15 (a)). Therefore, a temperature gradient was generated inside the sample. The bottom of the sample first reaches 660 °C, and the reaction generates a large amount of heat (Figure 15 (b)). Subsequently, the reaction heat was conducted to the upper part and further induced the reaction (Figure 15 (b, c)). It is known that the sample during the SHS mode includes reacted zone, reaction, zone, preheated zone, and unreacted zone. Al_3Ti are formed in the reaction zone and the reaction heat preheats the neighboring zone [19]. The self-propagating reaction reached the top (Figure 15 (d)). However, the reaction heat generated at the top is used to increase the temperature of the top itself (Figure 15 (d, e)). This is because there is no further part with lower temperatures (preheating and unreacted zones), which can receive the reaction heat. As a result, the temperature of the top increases significantly (Figure 15 (e)) to the melting temperature of the Al_3Ti phase. Then, the foaming starts by the melting of the matrix (Figure 15 (f)). In addition, the melting of the Al_3Ti phase promotes the secondary combustion reaction described in Equation (2) by the presence of Ti in the liquid phase (Figs. 10 (e) and 14) to generate a large amount of heat (Figure 15 (f)). Then, the upper part is reacted and reaction zones. The secondary reaction also self-propagated to the lower part (preheating and unreacted zones for the secondary reaction) and quenched. It is known that the temperature at the interface between reacted and unreacted zones needs to reach the melting temperature of reactant elements (melting temperature of Al_3Ti phase, in the case of this study) for self-propagating the reaction throughout the sample. In the present study, heating was stopped when the expansion of the bottom was observed. Therefore, the interfacial temperature would be below the melting temperature of Al_3Ti phase, resulting in stopping the self-propagation.

It can be concluded that the foaming at the side opposite to the heated end was due to the difference in triggers for the combustion reactions in Eqs. (1) and (2) (melting of Al and Al_3Ti). Arakawa et al. reported that foaming occurred from the heated part of a long-scale precursor [41]. The difference in the first foamed part was caused by the heating manner and sample size. In the previous study [41], the end of the long-scale precursor was heated before foaming.

However, in the present study, heating was stopped when the expansion of the bottom was observed to prevent foaming of the small sample under the TE mode. As a result, the heated part was not foamed first because the temperature did not reach the melting temperature of the Al_3Ti phase.

The discussion above indicates that the SHS-mode foamed sample in the present study includes the graded microstructures corresponding to each combustion foaming behavior of gradual expansion, temporary steady state at a constant volume, slight shrinkage before foaming, and rapid foaming. Therefore, the reaction process corresponding to the TE-mode foaming behavior is discussed below based on the microstructure in the SHS-mode foamed sample.

Figure 16 shows a schematic illustration of the foaming and reaction processes during the combustion foaming of porous Al_3Ti composite from Al–Ti– B_4C powders. When the precursor is heated to $660\text{ }^\circ\text{C}$, the Al powder melts. Takata et al. reported that, in the combustion reaction between Al and Ti, the Al_3Ti phase was first formed by the dissolution of Ti into molten Al owing to the faster diffusion and solubility of Ti in the liquid phase [42]. Wang et al. reported that Al_3Ti formed prior to the formation of any other titanium aluminides present in the Al–Ti system by depositing molten Al droplets onto the Ti powders layer at $350\text{ }^\circ\text{C}$ [43]. In the present study, Al_3Ti phase is first formed via the fast dissolution of Ti into molten Al (red arrow in the second figure of the reaction process). The formation and growth of the Al_3Ti phase around the Ti particles could generate voids and expand the sample [40] (third figures of the foaming and reaction processes). It is considered that the Ti_3Al phase would be formed by the solid–solid reaction between Ti and Al_3Ti phases [39]. The dissipation of molten Al due to the formation and growth of the Al_3Ti phase with a high melting temperature inhibits the further progress of the combustion reaction owing to slower diffusion in solid phases (third figure of the reaction process). Shen et al. revealed that the addition of Al to the Ti– B_4C reactants significantly promotes the reaction between B_4C and Ti via the prior formed Al_3Ti layer, which provides an easy route for mass transfer [39]. In the present study, TiB_2 was formed on B_4C and Al_3Ti

phases. TiB_2 is gradually formed by the solid–solid reaction between B_4C and Al_3Ti phases, which provide the temporary steady state at a constant volume (third and fourth figures of the foaming and reaction processes). The formation of TiB_2 (and TiC) gradually increases the sample temperature to the melting temperature of Al_3Ti phase. Partial melting of the Al_3Ti phase shrinks the sample and promotes the combustion reaction drastically by the dissolution of Ti into the liquid phase (red arrow in the fifth figure of the reaction process) and solid–liquid reaction between B_4C particles and Ti in the liquid phase (fifth figures of the foaming and reaction processes). Then, the sample foams drastically by releasing the gas and melting of most of the Al_3Ti matrix (sixth figures of the foaming process). The sample is solidified as a porous metal after experiencing the growth, combination, and disappearance of bubbles (seventh figures of the foaming process). The solidified sample reaches almost the equilibrium state consisting of Al_3Ti and TiB_2 (and TiC) phases (sixth figures of the reaction process).

Kanetake et al. reported that gases inside pores in porous Al-Ni fabricated by combustion foaming process include massive hydrogen [17]. Kobashi et al. revealed that the gas volume released from the Al-Ni sample during the combustion foaming increases with increasing the Al content [18]. Kim et al. reported that surface of Al powder under air is covered with hydrous oxide ($\text{Al}_2\text{O}_3 \cdot 3\text{H}_2\text{O}$), which is decomposed to release hydrogen by heating to approximately 500 °C [44]. These results suggest that the gas source for combustion foaming would be hydrogen gas released from the hydrous oxide ($\text{Al}_2\text{O}_3 \cdot 3\text{H}_2\text{O}$) covered on raw Al powder. Kamynina reported that the formation of foam is that the gas evolution must coincide in time with melting of the sample [30]. However, the ignition temperatures in the present study were approximately 660 °C and 1340 °C, which is higher than 500 °C, leading to the fact that the gas evolution did not coincide with melting of the sample. One of the possibilities to solve the discrepancy is the trap of gases inside the sample before foaming. Kobashi et al. reported that lower relative density led to lower porosity of porous Al-Ni fabricated by combustion foaming

[45], which suggests that the gases released from the hydrous oxide might escape out of the precursor with low relative density before foaming. To clarify the nature of foaming, further investigation such as in-situ monitoring of gases released from the samples is needed.

Arakawa et al. reported that preheating at 350 and 400 °C homogenizes the porous structure in SHS processed porous Al_3Ti composite [41]. This previous study indicates that the uniformity of the temperature in the specimen is important for obtaining a homogeneous porous structure. In the present study, it was revealed that the sample experienced an incubation period (temporary steady state at constant volume) before foaming owing to a slow solid–solid reaction. The solid–solid reaction can generate nonuniform temperature distribution, leading to a coarse and inhomogeneous porous structure, as shown in Figure 5 (a). Therefore, there is a possibility that the porous structure can be controlled not only by preventing the coarsening of bubbles after foaming, but also by the reaction before foaming, which is affected by the composition of the Al–Ti– B_4C powders and the heating manner. Further investigations are required for verification.

5. Conclusion

The combustion foaming behaviors (the TE mode and SHS mode) in the synthesis of the porous Al_3Ti composite were observed in situ using X–ray radioscopy. Furthermore, microstructures were characterized to better understand the chemical reactions causing the combustion foaming behaviors. The main findings are summarized as follows:

- The combustion foaming process consists of six steps: (1) gradual expansion, (2) temporary steady state at a constant volume, (3) slight shrinkage, (4) rapid foaming, (5) severe shrinkage and bubble coarsening, and (6) solidification.
- The temporary steady state caused by the difference in the ignition temperature of two reactions to form Al_3Ti and TiB_2+TiC . A solid–solid reaction to form TiB_2 (and TiC)

between the B_4C and Al_3Ti phases increase the sample temperature to melting temperature of Al_3Ti phase, resulting in the rapid foaming.

- During foaming, bubbles are generated in the sample and are then dissipated, combined, and coarsened. The bubbles remain as large pores in the sample consisting of Al_3Ti and TiB_2 (and TiC) phases.

References

- [1] L. J. Gibson and M. F. Ashby, *Cellular Solids Structure and Properties - second edition*, Cambridge Solid State Science Series **1999**.
- [2] J. Banhart, *Prog. Mater. Sci.* **2001**, *46*, 559.
- [3] T. S.-Chung, M. W.-Ping, *Int. J. Adv. Manuf. Technol.* **2007**, *32* 473.
- [4] T. Miyoshi, M. Itoh, S. Akiyama, A. Kitahara, *Adv. Mater. Eng.*, **2000**, *2*, 179.
- [5] C. M. W.-Close, R. Minor, J. Doorbar, *Intermetallics* **1996**, *4*, 217.
- [6] M. G. Mendiratta, S. K. Ehlers, D. M. Dimiduk, W. R. Kerr, S. Mazdiyasn, H. A. Lipsitt, *Mat. Res. Soc. Symp. Proc.* **1987**, *81*, 393.
- [7] W. Wu, *Intermetallics*, **2006**, *14*, 1114.
- [8] M. Sujata, S. Bhargava, and S. Sangal, *ISIJ Int.*, **1996**, *36*, 255.
- [9] M. Yamaguchi, Y. Umakoshi, T. Yamene, *Philo. Mag. A*, **1987**, *55*, 301.
- [10] N. Inoguchi, M. Kobashi, N. Kanetake, *Mater. Trans.* **2009**, *50*, 2609.
- [11] K. Morsi, *Mater. Sci. Eng. A* **2001**, *299*, 1.
- [12] M. Kobashi, S. Miyake, N. Kanetake, *Intermetallics* **2013**, *42*, 32.
- [13] X. Jiao, X. Wang, X. Kang, P. Feng, L. Zhang, J. Wang, F. Akhta, *Mater. Lett.* **2016**, *181*, 261.
- [14] Y. Shu, A. Suzuki, N. Takata, M. Kobashi, *J. Mater. Proc. Tech.* **2019**, *264*, 182.
- [15] M. Kobashi, R.-X. Wang, Y. Inagaki, N. Kanetake, *Mater. Trans.*, **2006**, *47*, 2172.

- [16]I. Barin, F. Sauert, E. S.-Rhonhof, W. S. Sheng, *Thermochemical Data of Pure Substances Part I and II*, VCH Verlagsgesellschaft mbH **1993**.
- [17]N. Kanetake, M. Kobashi, *Scrip. Mater.* **2006**, *54*, 521.
- [18]M. Kobashi, N. Kanetake, *Adv. Eng. Mater.* **2002**, *4*, 745.
- [19]A. Varma, A.S. Rogachev, A.S. Mukasyan, S. Hwang, *Adv. Chem. Eng.*, **1998**, *24*, 79.
- [20]A. Delgado, S. Cordova, I. Lopez, D. Nemir, E. Shafirovich, *J. Alloys Compd.* **2016**, *658*, 422.
- [21]M. Shekari, M. Adeli, A. Khobzi, M. Kobashi, N. Kanetake, *Adv. Powder Tech.* **2017**, *28*, 2974.
- [22]M. Kobashi, N. Kanetake, *Materials* **2009**, *2*, 2360.
- [23]F. G.-Moreno, M. Fromme, J. Banhart, *Adv. Eng. Mater.* **2004**, *6*, 416.
- [24]F. G.-Moreno, M. Mukherjee, C. Jiménez, A. Rack, J. Banhart, *Metals* **2012**, *2*, 10.
- [25]P. H. Kamm, F. G.-Moreno, T. R. Neu, K. Heim, R. Mokso, J. Banhart, *Adv. Eng. Mater.* **2017**, *19*,1600550.
- [26]F. G.-Moreno, P. H. Kamm, T. R. Neu, F. Bülk, R. Mokso, C. M. Schlepütz, M. Stampanoni, J. Banhart, *Nature Communications* **2019**, *10*, 3762.
- [27]Y. Arakawa, C. Jiménez, F. G.-Moreno, J. Banhart, A. Rack, M. Kobashi, N. Kanetake, *Proc. Mater. Sci.* **2014**, *4*, 268.
- [28]I. Ohuna, Y. Fujita, H. MituiI, K. Ishikawa, R. Kainuma, K. Ishida, *Acta Metall.* **2000**, *48*, 3113.
- [29]J. B. Holt, Z. A. Munir, *J. Mater. Sci.***1986**, *21*, 251.
- [30]O. K. Kamynina, S. G. Vadchenko, A. E. Sytshev, A. S. Rogachev, L. M. Umarov, N. V. Sachkova, *Int. J. Self-Propagating High-Temp. Synthesis* **2007**, *16*, 137.
- [31]P. Norby, A. N. Christensen, *Acta Chemica Scandinavica A.* **1986**, *40*, 157.
- [32]M. I. Aivazov, I. A. Domashnev, *Inorg. Mater., Translated From Izv.Akad. Nauk SSSR, Neorg. Mater.*, **1971**, *7*, 1551.

- [33]A. N. Christensen, *Acta Chemica Scandinavica A*. **1978**, 32, 89.
- [34]S. I. Wright, M. M. Nowell, S. P. Lindeman, P. P. Camus, M. D. Graef, M. A. Jackson, *Ultramicroscopy* **2015**, 159, 81.
- [35]N. Schmitz-Pranghe , P. Dünner, *Zeitschrift fuer metallkunde*, **1968**, 59, 377-38.
- [36]H. L. Yakel, *Acta Cryst*, **1975**, B31, 1797.
- [37]A. Penalzoza, C. R. Houska, Refinements on the X-ray Intensities from Ti₃₋₂Al, An Congr. Nac. Metal. **1983**, 3, A54.
- [38]H. Wang, R.C. Reed, J.C. Gebelin, N. Warnken, *Comput. Coupling Phase Diagrams Thermochem.*, **2012**, 39, 21.
- [39]P. Shen, B. Zou, S. Jin, Q. Jiang, *Mater. Sci. Eng. A* **2007**, 454–455, 300.
- [40]A. Hibino, R. Watanabe, *J. Japan Inst. Metals* **1991**, 55, 1256.
- [41]Y. Arakawa, M. Kobashi, N. Kanetake, *Intermetallics*, **2013**, 41, 22.
- [42]N. Takata, K. Uematsu, M. Kobashi, *Mater. Sci. Eng. A* **2017**, 697, 66.
- [43]P.-Y Wang, H.-J Li, L.-H Qi, X.-H, Zheng, H.-S Zuo, *Prog. Natural Sci. Mater. Int.* **2011**, 21, 153.
- [44]Y. -M. Kim, W. M, Griffith, F. H. Froes, *JOM* **1985**, 37, 27.
- [45]M. Kobashi, R. -X Wang, Y. Inagaki, N. Kanetake, *Mater. Trans.* **2006**, 47 2172.

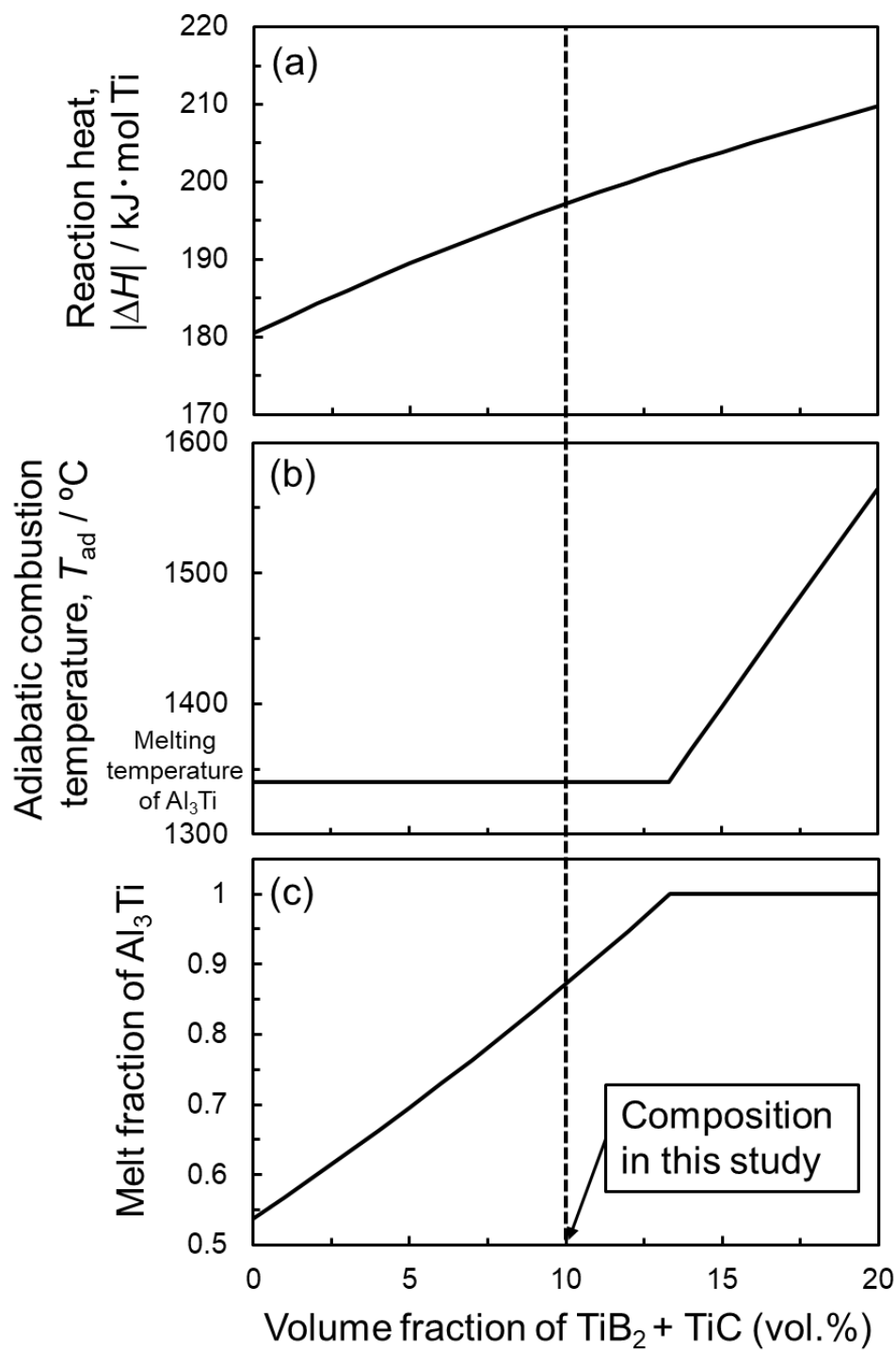


Fig. 1 Changes in (a) total reaction heat, (b) adiabatic combustion temperature, and (c) melt fraction of Al_3Ti phase as a function of the total volume fraction of TiB_2 and TiC .

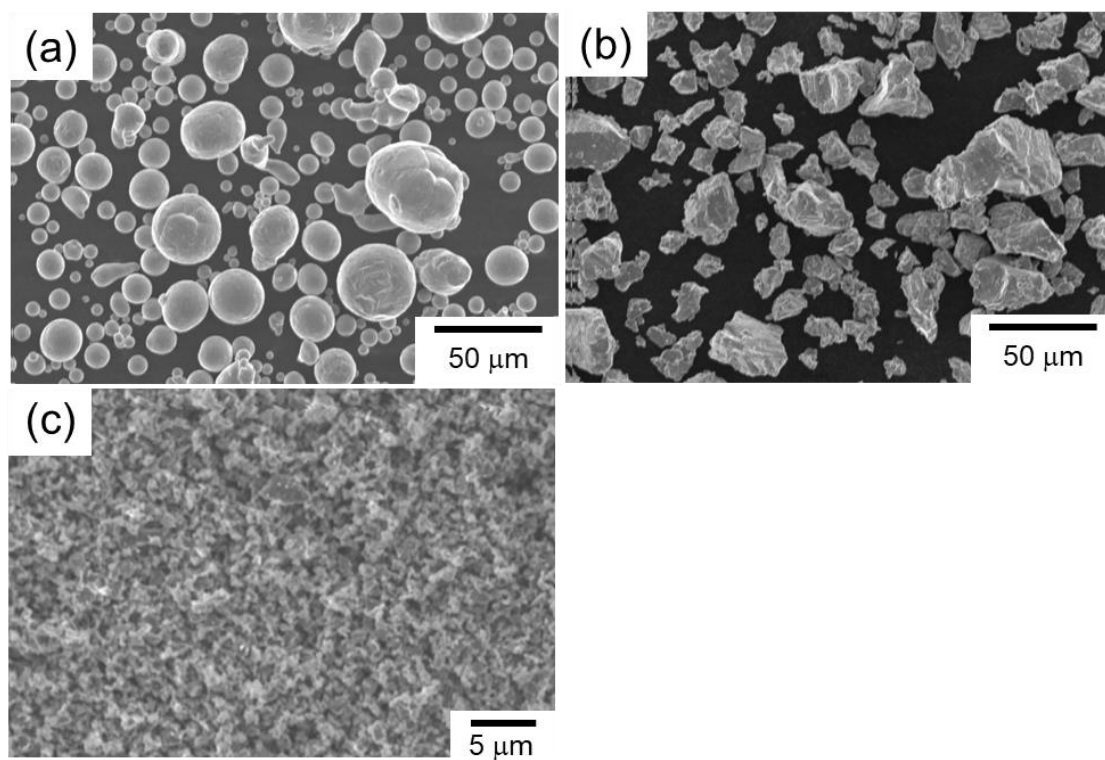


Fig. 2 Secondary electron images (SEIs) of initial powders; (a) Al, (b) Ti, and (c) B₄C.

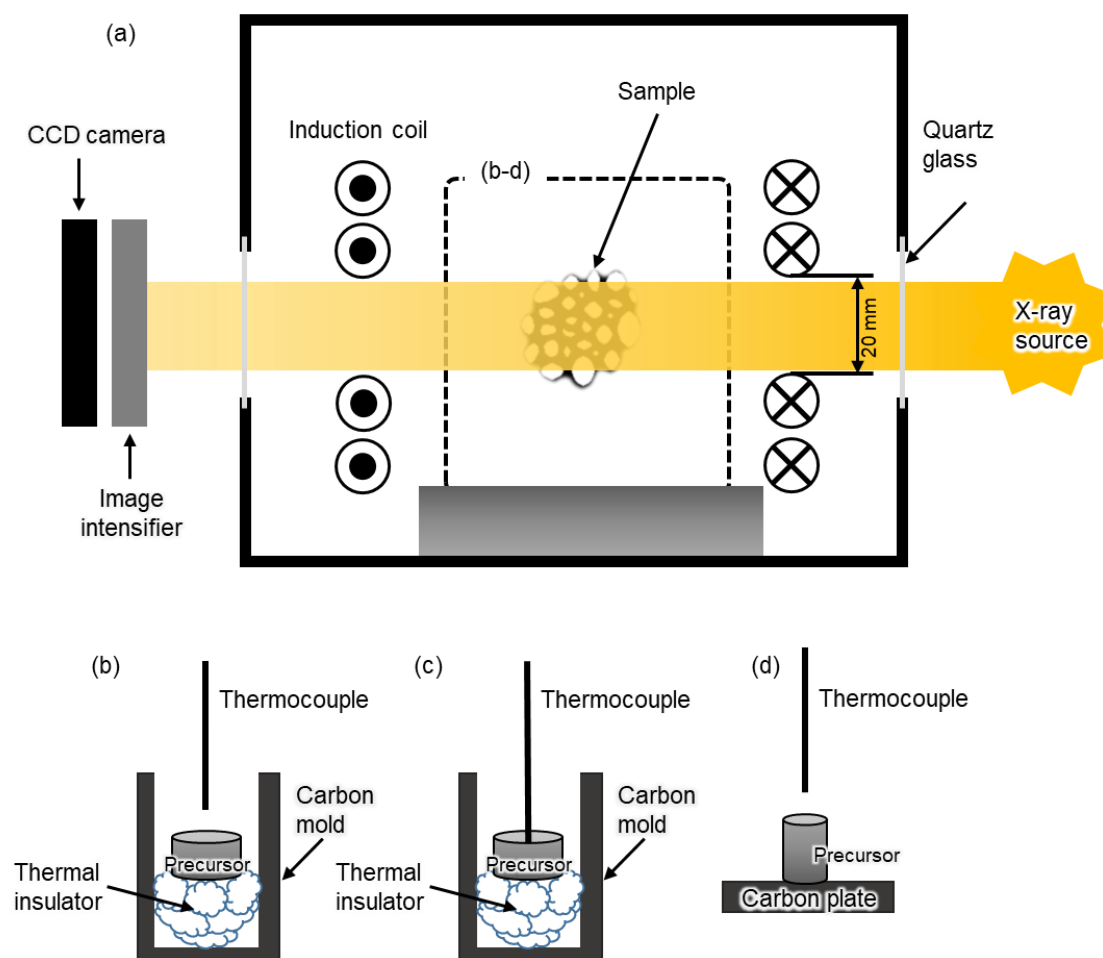


Fig. 3 Schematic illustrations showing (a) in-situ X-ray observation during heating samples using a high-frequency induction furnace, and (b-d) the set-up around the samples foamed under (b, c) TE and (d) SHS modes for (b, d) in-situ observation and (c) measurement of sample temperature.

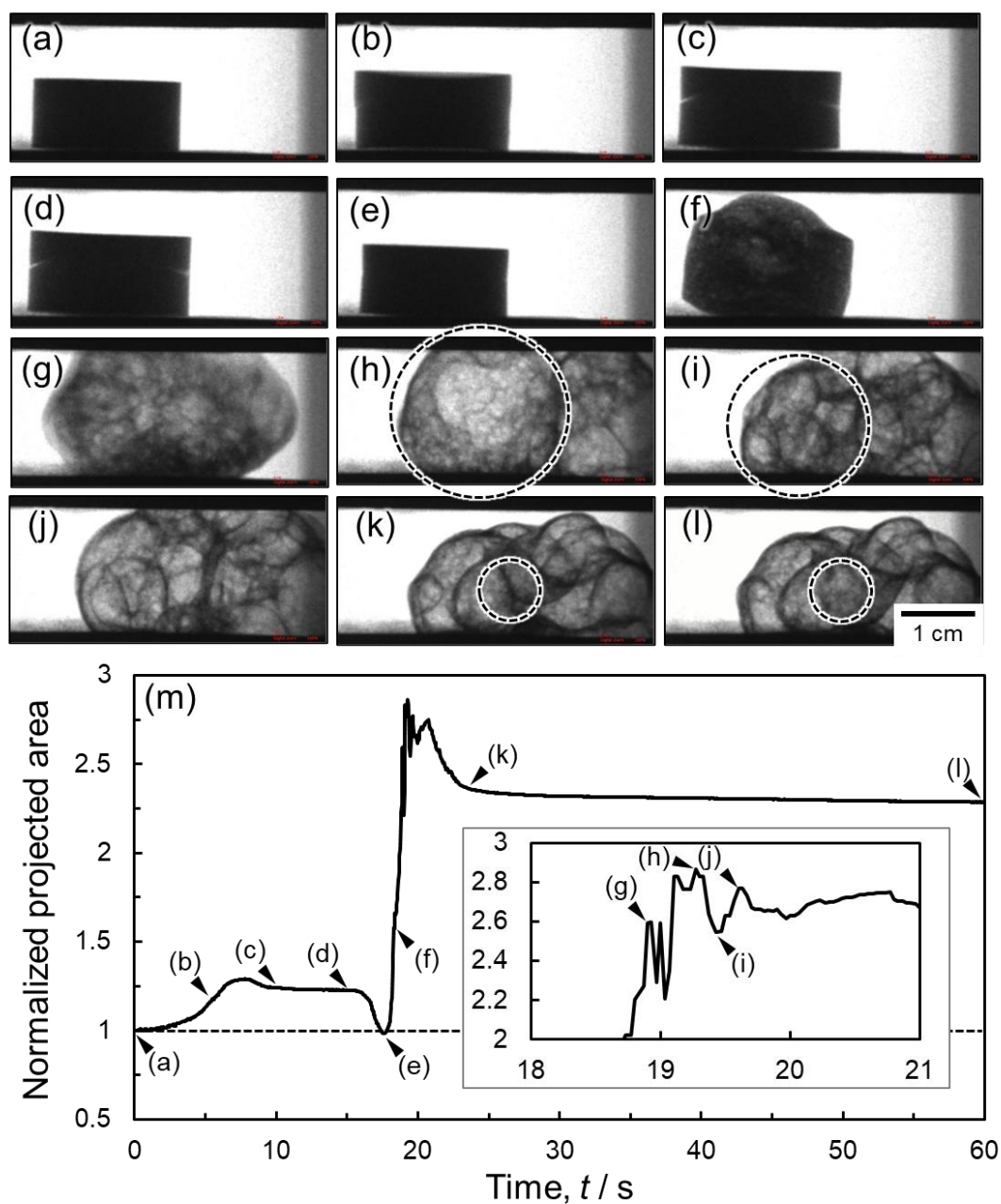


Fig. 4 X-ray radiography images showing foaming process of the TE mode sample at (a) 0.0 s, (b) 5.4 s, (c) 10.0 s, (d) 15.0 s, (e) 17.4 s, (f) 18.1 s, (g) 18.6 s, (h) 19.1 s, (i) 19.9 s, (j) 20.9 s, (k) 23.5 s, and (l) 59.7 s. (m) Change in projected area normalized by the projected area of the precursor in (a) as a function of time.

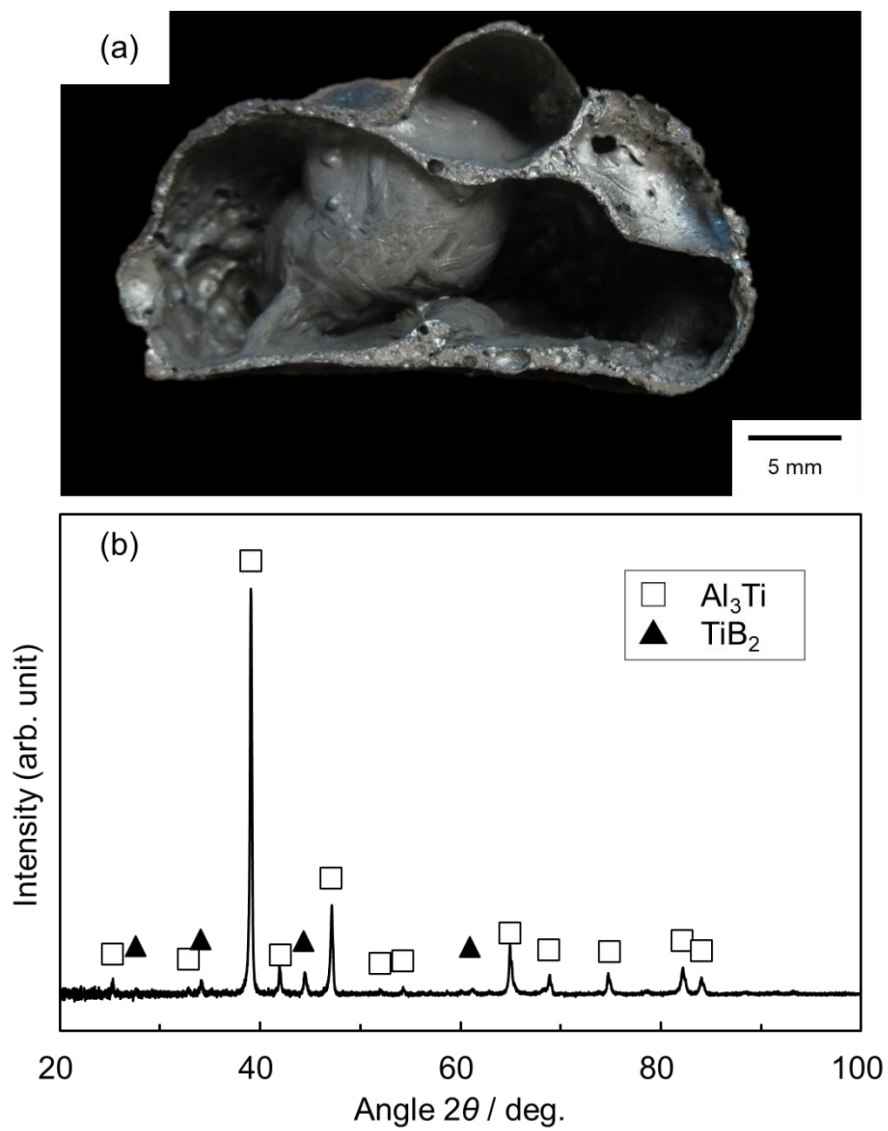


Fig. 5 (a) Photograph showing the cross-section of the porous Al₃Ti composite fabricated through the foaming process shown in Fig. 4. (b) X-ray diffraction (XRD) profile of the sample.

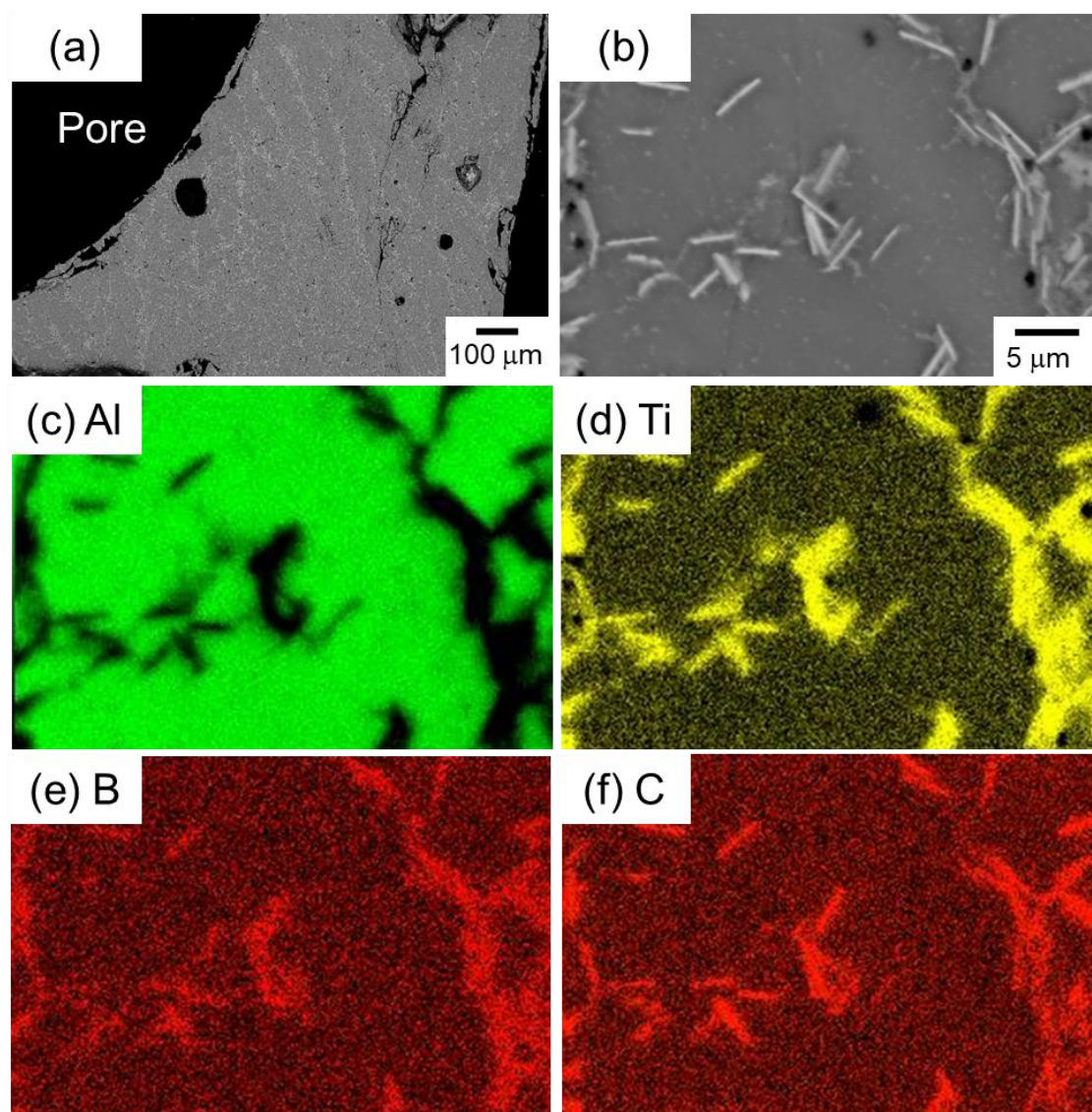


Fig. 6 (a) Low- and (b) high-magnification backscattered electron images (BEIs) showing the microstructure and (c–f) EDS element maps of (c)Al, (d)Ti, (e) B, and (f) C in the sample foamed under the TE mode shown in Fig. 4.

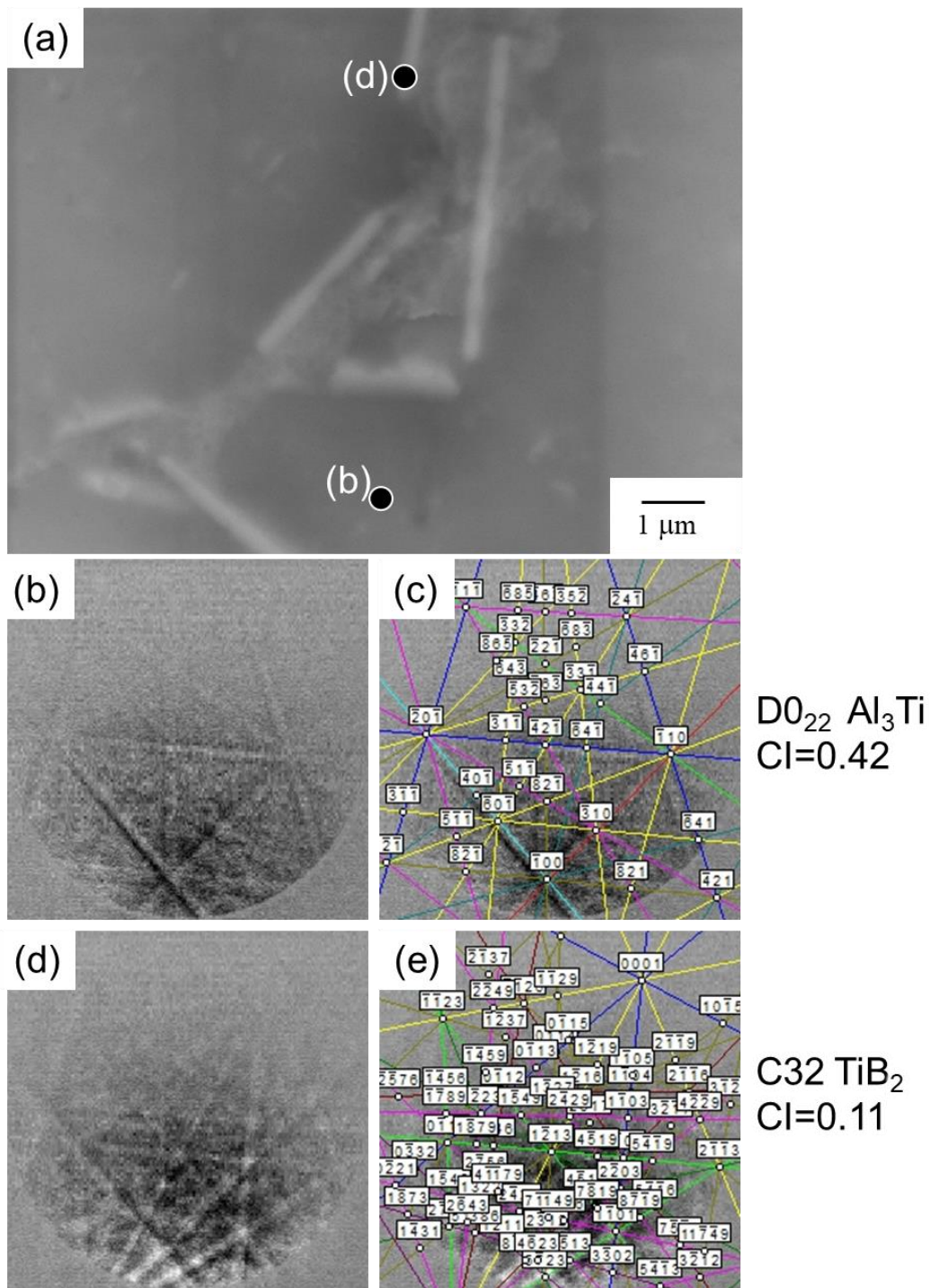


Fig. 7 (a) Field emission SEM (FE-SEM) showing the electron backscattered diffraction (EBSD) analysis points in the sample foamed under the TE mode, (b, d) EBSD patterns from the points shown in (a), and (c, e) their fitted images. The fitted phases and confidence index (CI) values are also shown.

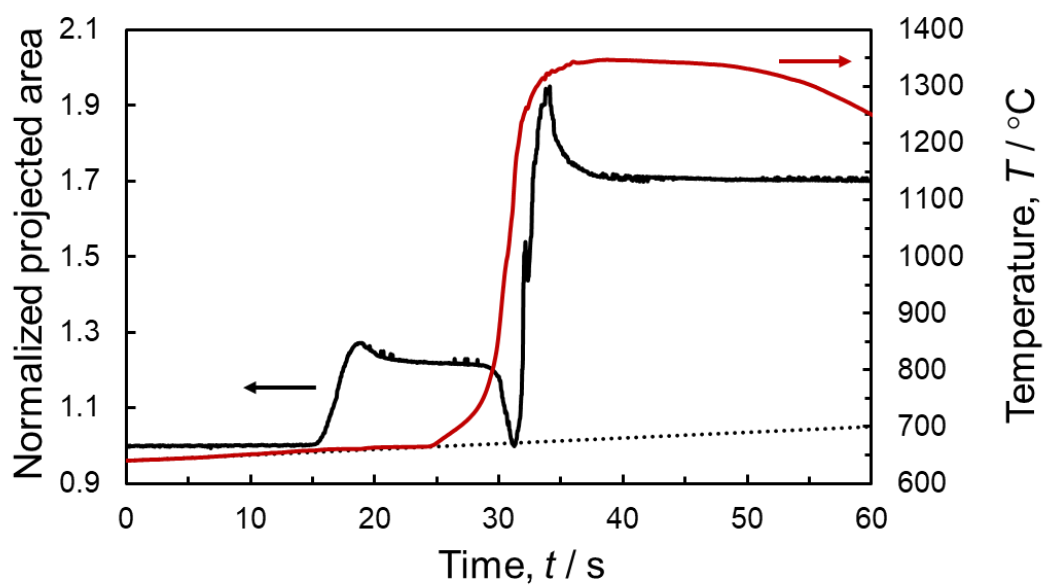


Fig. 8 Changes in projected area normalized by the projected area of the precursor and temperature measured with a thermocouple inserted into the sample as a function of time.

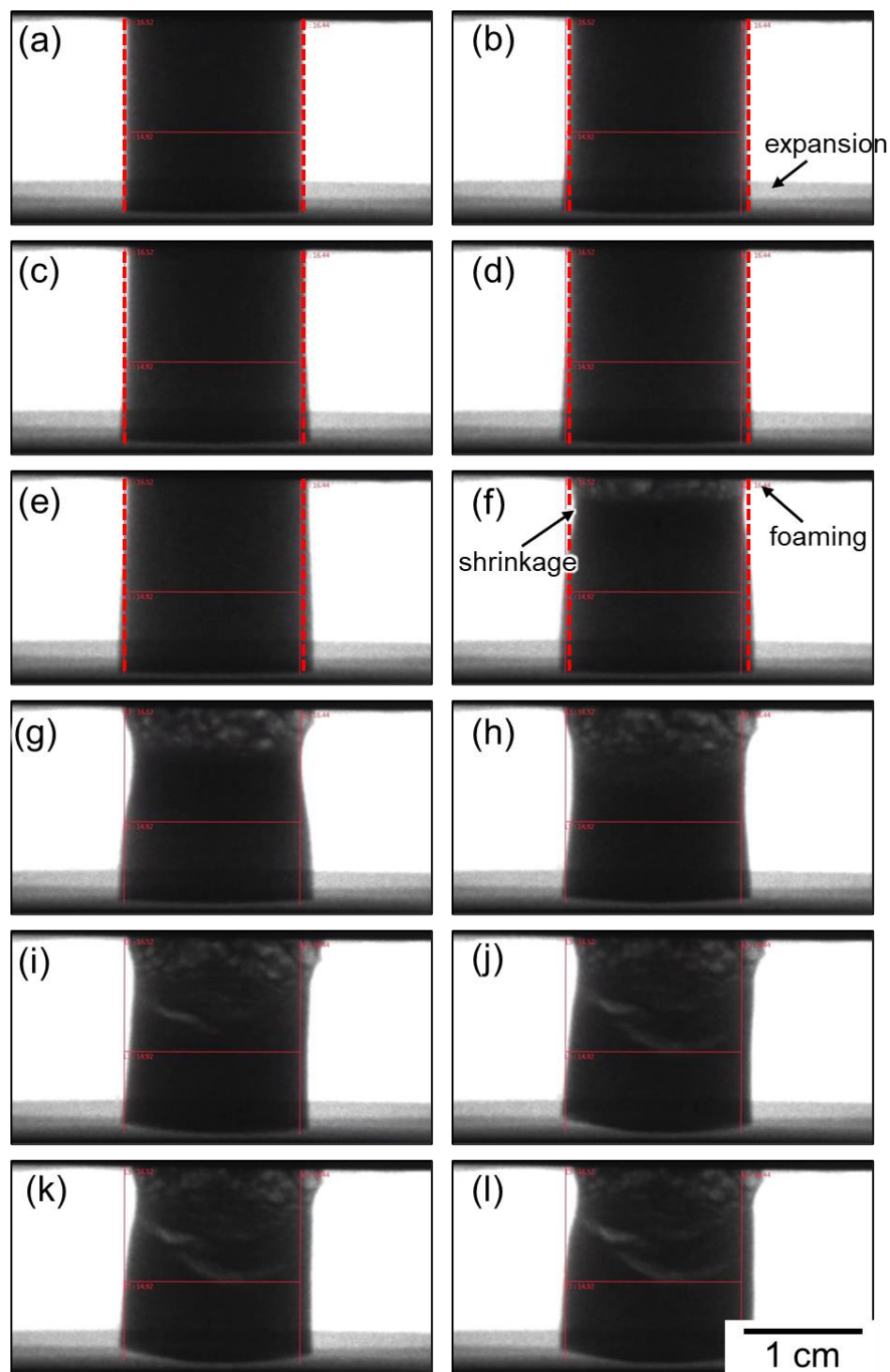


Fig. 9 X-ray radiography images showing foaming process of SHS mode at (a) 0.0 s, (b) 50.0 s, (c) 60.0 s, (d) 70.0 s, (e) 86.0 s (f) 87.0 s, (g) 88.0 s, (h) 90.0 s, (i) 93.0 s, (j) 100 s, (k) 120.0 s, and (l) 180.0 s.

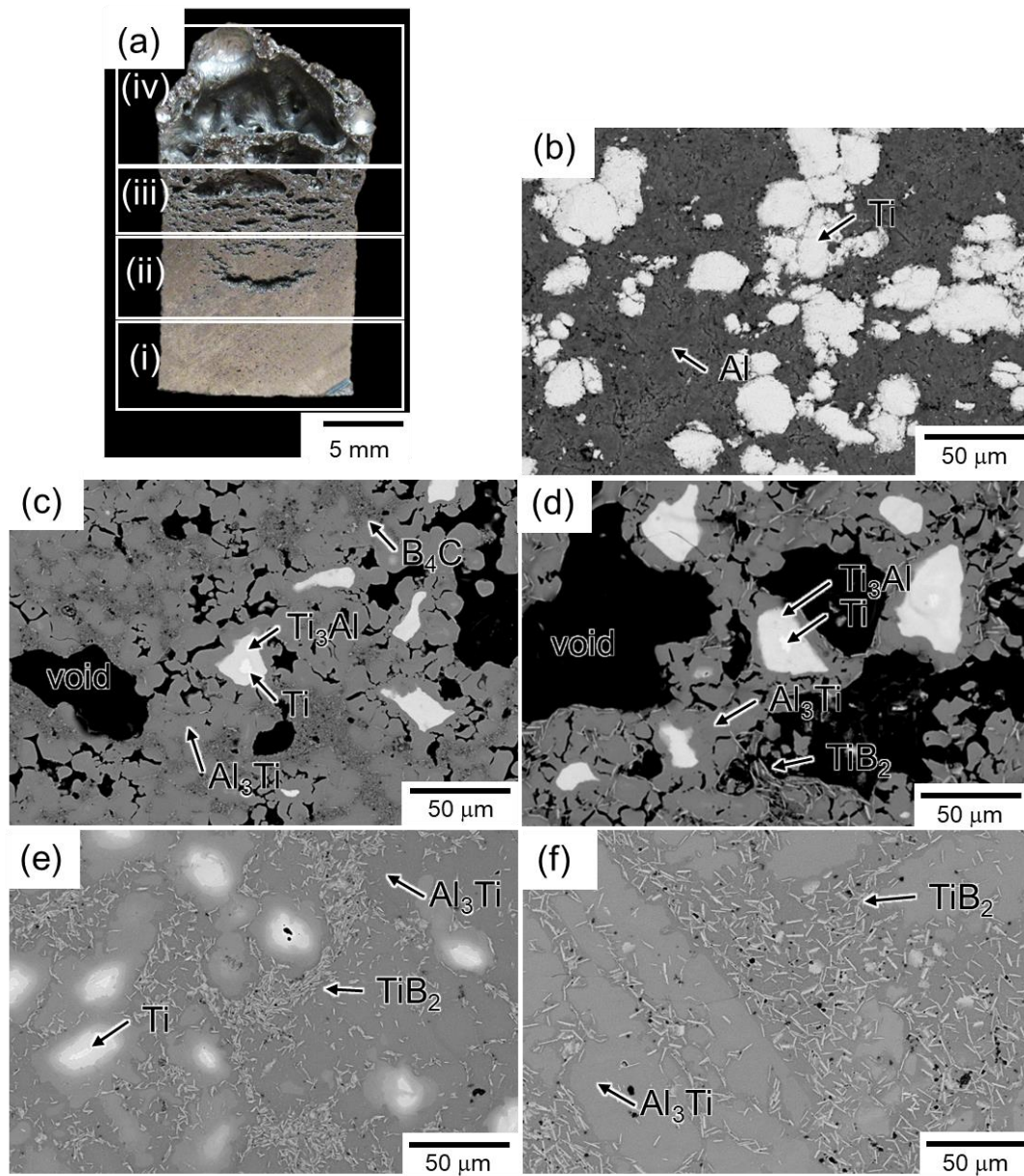


Fig. 10 (a) Photograph showing cross section of the SHS-mode foamed sample. (b–e) SEM images of (b) precursor, (c) region (i), (d) region (ii), (e) region (iii), and (f) region (iv).

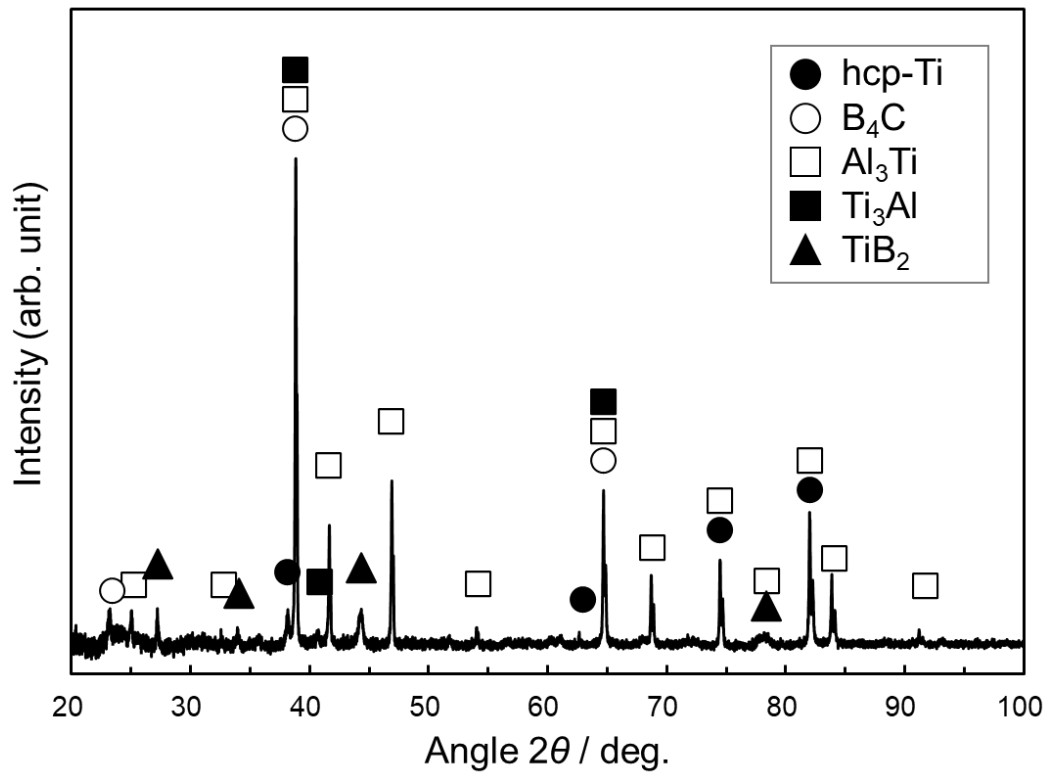


Fig. 11 XRD profile measured at region (i) shown in Fig. 10 (a).

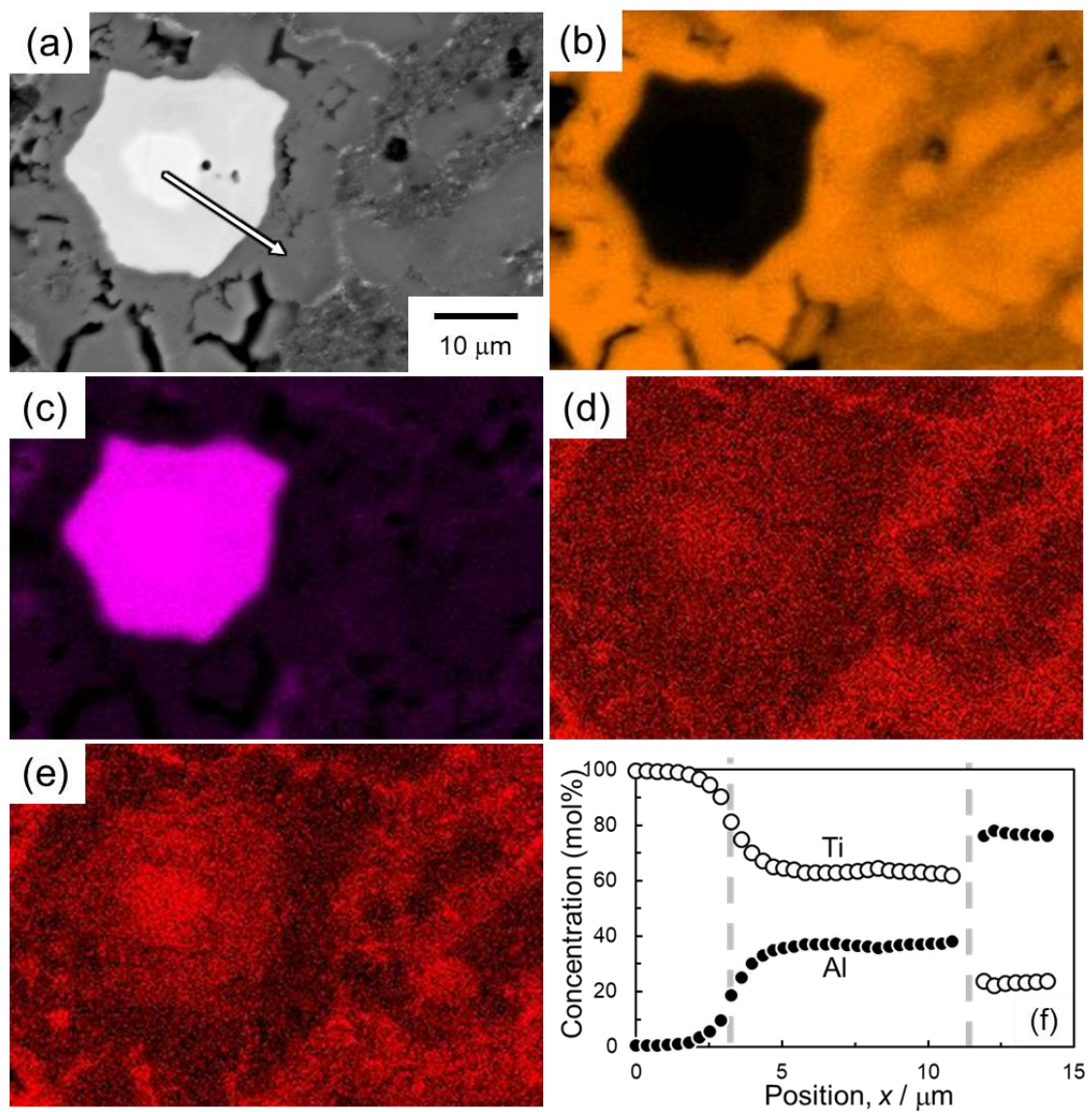


Fig. 12 (a) High-magnification BEI for region (i) in Fig. 10 (a) and (b–e) EDS element maps of (b) Al, (c) Ti, (d) B, and (e) C. (f) Concentration profiles of Al and Ti measured along the white arrow in (a).

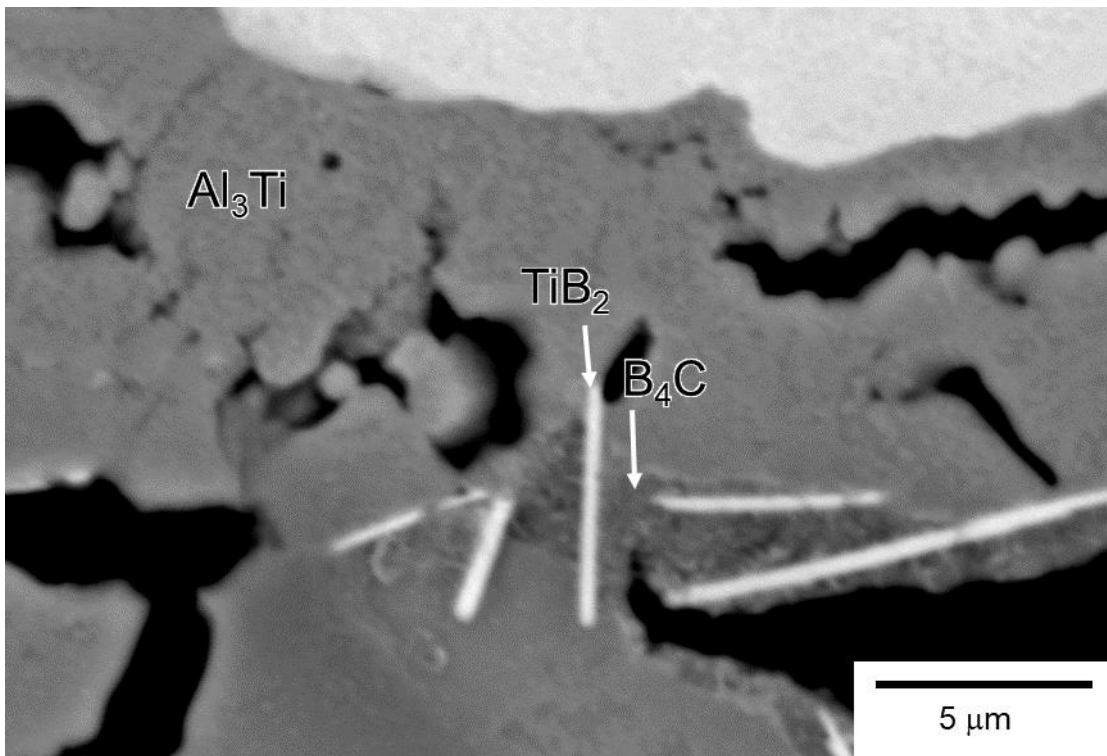


Fig. 13 High-magnification BEI showing the microstructure at region (ii) in Fig. 10 (d).

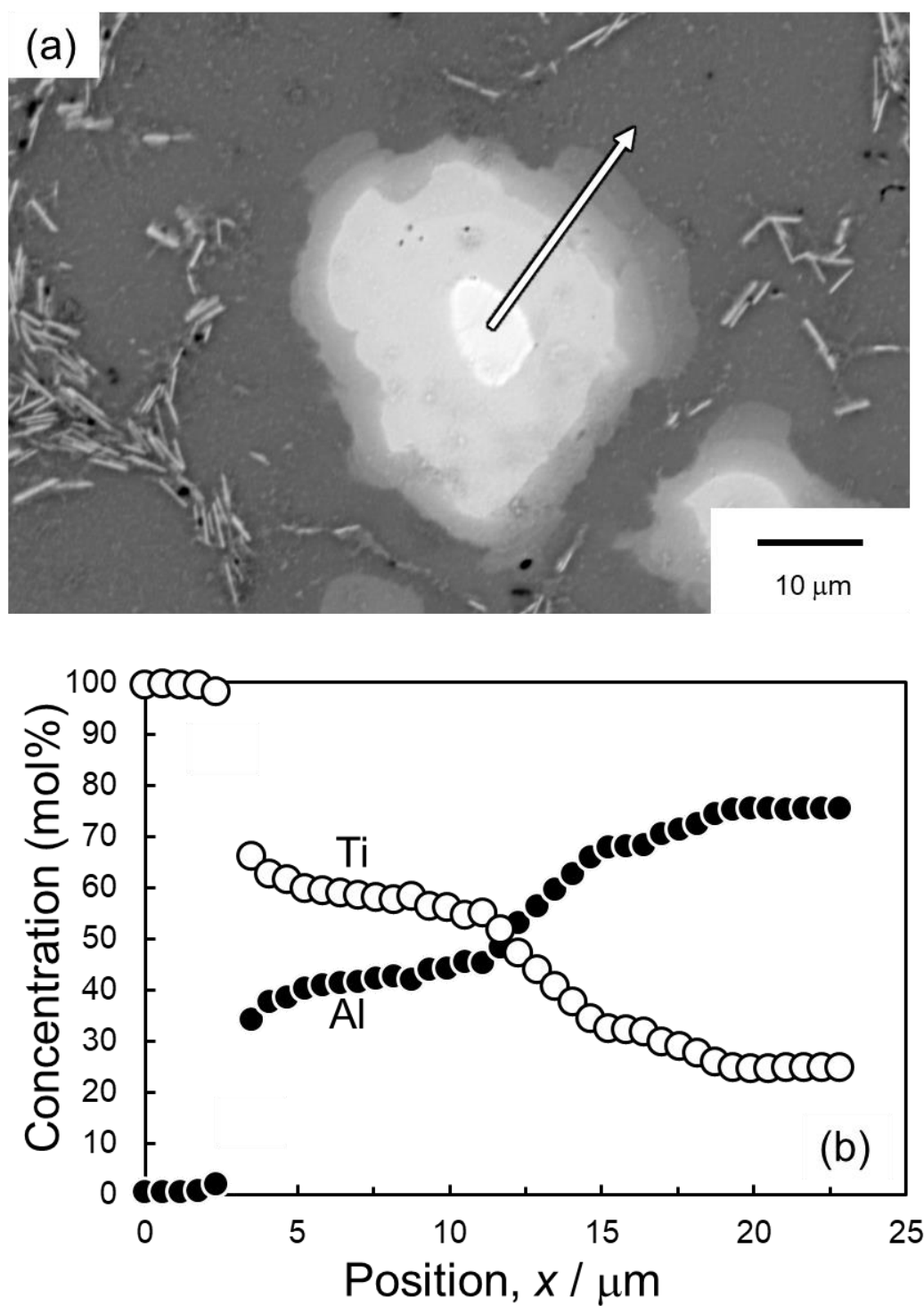


Fig. 14 (a) High-magnification BEI of the region (iii) in Fig. 10(e) showing the position for EDS line analysis and (b) concentration profile along the white arrow in (a) obtained by the EDS analysis.

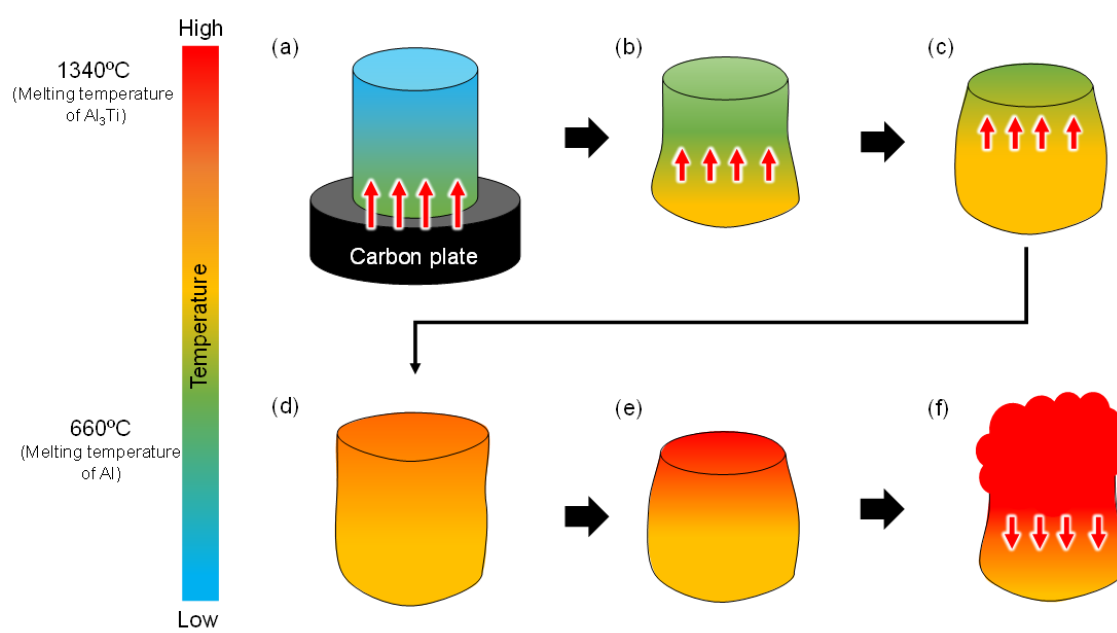


Fig. 15 Schematic illustration showing heat flow during SHS foaming process observed in situ using X-ray radiography.

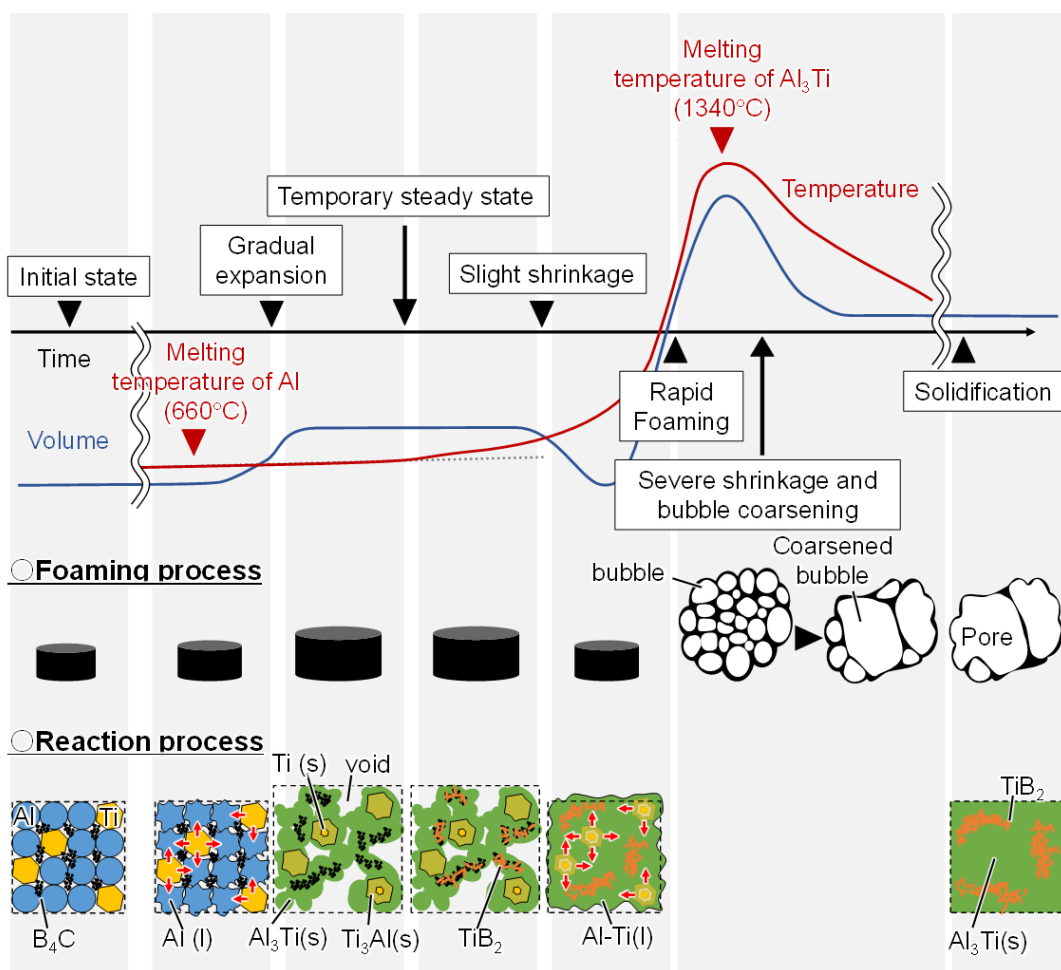


Fig. 16 Schematic illustration showing the foaming and reaction processes during combustion foaming of porous Al₃Ti composite from Al-Ti-B₄C powder mixture.